Electrochimica Acta 517 (2025) 145763

Contents lists available at ScienceDirect

Electrochimica Acta

journal homepage: www.journals.elsevier.com/electrochimica-acta

Innovative biochar-based electrocatalysts from chilli plants and fruits for sustainable oxygen reduction and hydrogen evolution reactions

Sumanth Dongre S[a], Giovanni Zuccante[b,c], Mohsin Muhyuddin[b], Carmelo Lo Vecchio[d], Vincenzo Baglio[d], Enrico Berretti[e], Alessandro Lavacchi[e], Shwetharani R[a], R. Geetha Balakrishna[a], Carlo Santoro[b,*]

[a] *Centre for Nano and Material Sciences (CNMS), Jain (Deemed-to-be University), Ramanagara, 562112, Karnataka, India*
[b] *Electrocatalysis and Bioelectrocatalysis Lab, Department of Materials Science, University of Milano-Bicocca, U5, Via Cozzi 55, 20125, Milano, Italy*
[c] *Department of Industrial Engineering, University of Padova, Via Marzolo 9, Padova, 35131, Italy*
[d] *Institute for Advanced Energy Technologies "Nicola Giordano" CNR-ITAE, Via Salita S. Lucia sopra Contesse 5, 98126 Messina, Italy*
[e] *Institute of chemistry of organometallic compounds, CNR–ICCOM, Via Madonna del Piano 10, 50019 Sesto Fiorentino, Florence, Italy*

ARTICLE INFO

Keywords:
Oxygen reduction reaction
Alkaline media
Platinum group metal-free electrocatalysts
Hydrogen evolution reaction
Biochar electrocatalysts

ABSTRACT

The rapid population growth and the subsequent energy demands have led to a surge in fossil fuel usage, resulting in unprecedented environmental challenges due to carbon emissions. Green hydrogen seems to be a promising avenue to tackle the negative effects of fossil fuels to achieve an environment-friendly and sustainable energy source. In this study, we present the development of iron and nickel-based electrocatalysts derived from biochar obtained from chilli plants and their fruits for cathodic oxygen reduction reaction (ORR) and hydrogen evolution reaction (HER). The biochar was produced by pyrolyzing the biomass at 600 °C and 800 °C, followed by KOH activation and functionalization with iron(II) phthalocyanine for ORR and nickel nanopowder for HER. Electrochemical tests in alkaline media (0.1 M KOH for ORR and 1 M KOH for HER) demonstrated significant electrocatalytic activity. The Plant-Fe 800 electrocatalyst achieved an onset potential of 0.97 V (vs RHE) and a half-wave potential of 0.87 V (vs RHE) for ORR with minimal peroxide yield. For HER, the Chilli-Ni 800 electrocatalyst showed an overpotential of roughly 0.41 V (vs RHE). The high performance of these biochar-based electrocatalysts can be attributed to their large surface area, effective Fe-N_x active site dispersion, and the presence of nitrogen-related defects within the carbon matrix. This study highlights the potential of using sustainable, biomass-derived materials to create efficient and cost-effective electrocatalysts, paving the way for green energy.

1. Introduction

With a continuous increase in population, the energy demand is also growing exponentially day by day. The prime reliance on non-renewable energy sources like fossil fuels, also being on the brink of extinction, is causing a surge in carbon emissions leading to numerous negative impacts on the environment and disrupting the ecosystem [1]. Such a scenario triggers a search for more suitable and sustainable sources of energy to replace fossil fuels. Green hydrogen seems to offer a promising solution for addressing the harmful impacts of fossil fuels, paving the way toward sustainable and environmentally friendly energy alternatives [2]. With at least two times higher energy density compared to traditional fossil fuels, hydrogen could be an essential asset in helping the International Energy Agency (IEA) and various countries to reach their target of zero net carbon dioxide emissions by 2050 [3]. Among various processes of producing hydrogen, water electrolysis stands alone being a simple and efficient method of producing pure green hydrogen [4,5]. The economic utilization of produced green hydrogen is also equally important to leverage its full potential. Green hydrogen is efficiently produced by low-temperature water electrolysis (WE) technologies.

In this context, low-temperature fuel cells (FCs) with unprecedented potential to convert hydrogen into useful electrical energy without any carbon emission appear to be a step towards sustainability. FCs provide high energy conversion efficiency with minimal carbon emissions, potentially bridging the gap between increasing energy needs and

---

[*] Corresponding author.
E-mail address: carlo.santoro@unimib.it (C. Santoro).

https://doi.org/10.1016/j.electacta.2025.145763
Received 14 October 2024; Received in revised form 26 January 2025; Accepted 27 January 2025

environmental sustainability [6–8]. The slow kinetics and high overpotentials of cathode reactions in alkaline FCs and water electrolyzers (WEs), namely, oxygen reduction reaction (ORR) and hydrogen evolution reaction (HER) are hindering the full-scale implementation of these technologies. The scarcity and sky-rocketing prices of platinum group metals (PGM), which are currently used as cathode materials also pose a significant barrier to commercialization [9,10]. As a result, significant research was dedicated to enhancing the efficiency of both cathodic reactions by replacing the costly PGMs with cost-efficient and easy to produce electrocatalyst materials.

Consequently, nitrogen-rich carbon derived from biomass with atomically dispersed transition metals (TM-N_x-Cs, where TM = Fe, Ni, Co, etc.) is gaining recognition as a promising alternative to PGM electrocatalysts for ORR, attracting significant interest from the scientific community [11–14]. Carbon stands out as an optimal support material for various electrocatalysts due to its excellent electronic conductivity, stability, cost-effectiveness, and versatile structure [15]. The defect-rich nature of the carbon matrix ensures a favorable platform for electrocatalytic performance. This carbon matrix not only supports the overall electrochemical activity but also with its high surface area and mesoporous environment, enhances the mass transport of gaseous reactants to the active sites [16,17]. Among the TMs, iron-based electrocatalysts have demonstrated high electrocatalytic efficiency for the ORR, attributed to their suitable electronic structure and effective interaction with oxygen when coordinated with nitrogen [13,18]. Similarly, concerning the HER, nickel, especially in the form of metallic nanoparticles and oxides, has shown potential in improving electrocatalytic performance for the HER, owing to its electronic structure, which is comparable to that of Pd and Pt, known for their effectiveness in hydrogen evolution [19–21].

The use of carbon matrix derived from sustainable sources, other than traditional petrochemical methods, is crucial for enhancing the cost-effectiveness of electrocatalysts. Notably, biomass-derived carbon is gaining significant attention from researchers due to its easy synthesis and the formation of a highly porous matrix with a large surface area [22,23]. Advances were made in this field, where carbons with high surface areas were successfully synthesized from various plant-based materials such as leaves[24,25], fruits[26,27], and shells[28,29], demonstrating their effectiveness as valuable carbon support for electrocatalysts. In general, biochar exhibits excellent chemical stability, optimal electrical conductivity, and considerable mass transport capabilities. The porous structure of biochar enables the functionalization (func.) with metal sources, creating active sites within the carbon framework that are highly efficient for catalytic applications [30,31]. Recently, numerous studies have been reported on the synthesis of high-performance cathodic electrocatalysts for the HER and ORR using similar methods [32,33].

In this study, carbon-rich biochar was prepared from dried and pyrolyzed chilli plants and fruits. These biomass-based materials are rich in capsaicin and secondary alkaloids, making them excellent carbon sources with abundant oxygen-containing functional groups, aromatic rings, and amine groups [34]. Particularly, the chilli fruits and plants used in this work were the “peperoncino piccante calabrese”, a local Italian variety. The high nitrogen content of capsaicin makes chilli-derived biochar particularly effective for nitrogen doping, which enhances electrocatalytic performance, especially for the oxygen reduction reaction (ORR), by creating nitrogen-related defects in the carbon structure that serve as active catalytic sites [35]. Additionally, it was reported that the amount of waste material during the harvesting of chilli crops can be higher than 18 % (including leaves, stems, seeds and defective fruits) and usually this waste is either landfilled or incinerated [36–39]. The utilization of chilli biomass can alleviate the food waste impact, which is responsible for 4.4 Gt of greenhouse gases annually generated, i.e. ca. 21 % of the global carbon footprint and therefore supports the circular economy by transforming agricultural waste into valuable biochar [40,41]. The derived biochars were functionalized with transition metals containing precursors and employed as an electrocatalyst for ORR and HER in alkaline media. The biochar was synthesized via controlled pyrolysis at two distinct temperatures, 600 °C and 800 °C. For ORR electrocatalysis, the biochar was initially activated with KOH, followed by functionalization through pyrolysis with 10 wt% iron(II) phthalocyanine (FePc). For HER electrocatalysis, the biochar was directly functionalized by pyrolysis with 30 wt% nickel nanoparticles powder, without prior KOH activation. The impact of various synthesis conditions (such as pyrolysis temperature) on the electrochemical performance in alkaline environments was thoroughly investigated. The outcomes of this study provide substantial contributions to the development of efficient electrocatalysts for ORR and HER, aiming to replace those based on precious metals.

2. Materials and methodology

2.1. Materials

Analytical grade potassium hydroxide (KOH; Merck), iron(II) phthalocyanine ($C_{32}H_{16}FeN_8$; Acros Organics), nickel nanopowder (Sigma; 99 %), isopropanol ($(CH_3)_2CHOH$), Nafion 5 % w/w in water and 1-propanol solution (Alfa Aesar) were used without purification. Ultra-high purity nitrogen and oxygen gases were employed during the experiments. The experiments utilized ultrapure deionized water, produced using a Millipore Milli-Q system. Chilli plant and ripened chilli of the type “peperoncino piccante calabrese” were grown and collected from local premises (Milan, Italy).

2.1.1. Biochar production

The chilli plant and ripened chillies were initially recovered and washed with distilled water to remove soil remnants and other unwanted materials from the surface. The washed plant and chilli were dried for 72 hours at 80 °C to completely remove the moisture. The plant and chilli were crushed into powder separately and were pyrolyzed in a tubular furnace in 600 °C and 800 °C for 1 hour in N_2 atmosphere with a gas flow of 100 cm^3 min^{-1}. Both heating and cooling rates were maintained at 5 °C min^{-1}.

2.1.2. Synthesis of Fe functionalized char

To enhance the surface area and surface-active sites, the biochar was activated before functionalization. The char was stirred in 30 mL KOH-ethanol solution with KOH/biochar mass ratio of 4 for about 12 hours. Following the stirring, the solution was dried under N_2 atmosphere with continuous stirring at 80 °C. The obtained mixture was pyrolyzed at 700 °C for 1 hour in N_2 atmosphere with a flow rate of 100 cm^3 min^{-1} and step size of 5 °C min^{-1}. The product was washed with 1 M HCl solution followed by Milli-Q water until a neutral pH was achieved. The activated biochar was dried, crushed and collected for functionalization. The activated biochar was uniformly crushed with 10 wt.% iron(II) phthalocyanine (FePc) using agate mortar and pestle. The functionalization reaction was again carried out in a tubular furnace at 600 °C for 1 hour in H_2 atmosphere. Once the furnace was cooled down, the final sample was collected and stored for further analysis (Fig. 1).

2.1.3. Synthesis of Ni functionalized char

The synthesis of nickel-functionalized biochar electrocatalysts involved mixing biochar, obtained from the first pyrolysis, with 30 wt% nickel nanoparticle (NiNP) powder to achieve a homogeneous distribution of Ni particles within the carbon matrix. The Ni nanoparticles used in this study had a mean diameter of approximately 50 nm, as specified by the supplier. The homogenization process was carried out using a mortar and pestle to ensure uniform dispersion of the nanoparticles throughout the biochar. The mixture was then transferred to a tubular furnace in a ceramic boat for functionalization. The mixture was heated to 600 °C for 1 hour under flowing N_2 with a heating/cooling rate of 5 °C min^{-1}. The final, Ni functionalized samples were extracted and stored for further analysis. Notably, contrarily than Fe-based materials for ORR, KOH activation step was deliberately excluded during this synthesis of the Ni-functionalized samples. This was due to the fact that the carbon support cannot be too porous, otherwise during HER, hydrogen would form within the porosity avoiding water (main reagent) to reach the catalytic site. Formation of gases within porosity is able to strongly penalize the electrocatalytic activity and also reduce the stability of the materials. Additionally, prior studies have demonstrated that metallic Ni achieves sufficient interaction with the biochar matrix without requiring KOH activation, enabling the simplification of the synthesis process while maintaining effective HER activity [42] (Fig. 1, Table 1).

2.2. Instrumentations

The crystallographic phases were investigated with X-ray diffraction (XRD, Rigaku Miniflex 600, Tokyo, Japan) owning a Cu source. The XRD patterns were acquired in the range of 10–80° with a scan rate of 5°/min. The qualitative elemental analysis was carried out with an X-rays fluorescence (XRF, Artax 200, Bruker, Billerica, MA, USA) possessing a Mo anode. Elemental analysis was performed by using Elementar Vario Microcube Device. To study the surface morphology of the final materials, a desktop scanning electron microscopy (SEM, Thermo Fisher Phenom G6, Eindhoven, Netherlands) equipped with a thermoionic CeB6 source was used. The images were acquired in secondary electron (SE) mode. Samples were characterized using a Thermo Fisher Talos™ F200X G2 TEM, with Scanning TEM (STEM) and energy-dispersive X-ray analysis (EDX) capabilities. All the acquisitions were performed using a beam energy of 200 keV. To prepare the samples, a few drops of sample dispersions in isopropanol were drop-cast onto a Cu holey grid. Physical Electronics (PHI) 5800–01 X-ray photoelectron spectrometer was used to examine the surface characteristics of the plant and chilli-derived electrocatalysts. The instrument is equipped with an Alkα monochromatic X-ray source operating at a power of 350 W.

2.3. Electrochemical measurements

2.3.1. Preparation of electrocatalyst ink

The electrocatalyst inks were prepared by dispersing 5 mg of synthesized electrocatalyst sample in the mixture of 985 μL of isopropanol and 15 μL Nafion ionomer solution through sonication to attain a homogeneous electrocatalyst ink. For the measurements, about 0.6 mg cm^{-2} ink was drop-cast on the glassy carbon disk of the rotating ring disk electrode (RRDE) or rotating disk electrode (RDE) and dried at room temperature.

2.3.2. Oxygen reduction reaction (ORR) measurements

The electrochemical measurements were carried out in Pine WaveDriver 200 EIS Bipotentiostat coupled with Pine WaveVortex 10 rotating ring disk electrode (RRDE)/rotating disk electrode (RDE) setup. The RRDE was composed of a concentric glassy carbon disk (0.2376 cm^2 geometric area) and a Pt ring (0.2356 cm^2 geometric area) while the RDE had a glassy carbon disk with an area of 0.196 cm^2. The ORR analysis was carried out in a three-electrode system where, the RRDE coated with electrocatalyst was utilized as a working electrode, while a titanium wire and Ag/AgCl served as counter electrode and reference electrodes, respectively. Linear sweep voltammetry (LSV) was employed to investigate the ORR performance of the synthesized catalysts. In all electrochemical experiments, the potentials were converted to reversible hydrogen electrode (RHE) potential using the following equation,

$$E_{RHE} = E_{ref} + E^{o}_{ref} + 0.059 * pH \quad (1)$$

Where, E_{ref} denotes the working potential measured relative to the reference electrode and E^{o}_{ref} is the reference electrode's potential compared to the standard hydrogen electrode at 25 °C, which is 0.197 V for Ag/AgCl electrode. The ORR analysis was conducted in O_2 saturated 0.1 M KOH solution from 1 to 0 V vs RHE at a scan rate of 5 mV s^{-1}.

During the ORR measurements, the ring's potential was maintained at 1.2 V vs RHE and the currents produced by both the disk (I_{disk}) and the ring (I_{ring}) were measured. These values were then utilized to calculate the number of electrons exchanged, as described in Eq. (2), and to determine the amount of hydrogen peroxide formed, as outlined in Eq. (3).

$$n = \frac{4I_{disk}}{I_{disk} + \frac{I_{ring}}{N}} \quad (2)$$

Table 1
Name of the electrocatalysts studied and the synthesis steps followed.

Sample name	Biomass source	1st Pyrolysis 600 °C	1st Pyrolysis 800 °C	Activation	FePc func. (wt.%)	NiNP func. (wt.%)
Plant-Fe 600	Chilli Plant	✓		✓	✓ (10)	
Plant-Fe 800	Chilli Plant		✓	✓	✓ (10)	
Chilli-Fe 600	Chilli Fruits	✓		✓	✓ (10)	
Chilli-Fe 800	Chilli Fruits		✓	✓	✓ (10)	
Plant-Ni 600	Chilli Plant	✓				✓ (30)
Plant-Ni 800	Chilli Plant		✓			✓ (30)
Chilli-Ni 600	Chilli Fruits	✓				✓ (30)
Chilli-Ni 800	Chilli Fruits		✓			✓ (30)

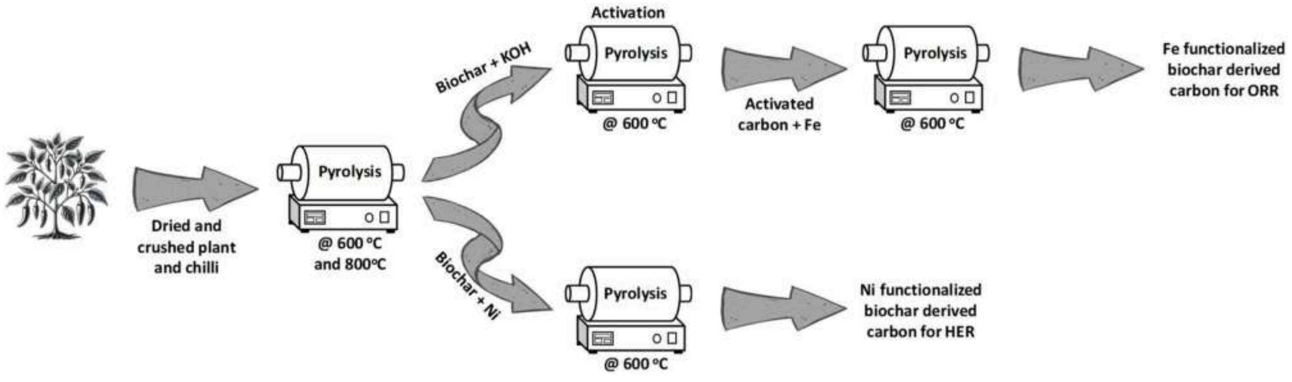

Fig. 1. Schematic illustration of the experimental design for the electrocatalyst synthesis.

$$H_2O_2\% = \frac{200\,\frac{I_{ring}}{N}}{I_{disk} + \frac{I_{ring}}{N}} \tag{3}$$

Where N is the current collection efficiency (0.38).

2.3.3. Hydrogen evolution reaction (HER) measurements

The HER analysis was also carried out in a three-electrode system where, the RDE coated with an electrocatalyst was utilized as a working electrode, while graphite rod and Ag/AgCl as counter electrodes and reference electrodes, respectively. The linear sweep voltammetry (LSV) was employed to investigate the HER performance of the synthesized electrocatalysts. In all electrochemical HER experiments, the potentials were converted to RHE potential using Eq. (1). The HER analysis was conducted in N_2 saturated 1 M KOH solution from 0 to −1 V vs RHE at a scan rate of 5 mV/s.

3. Results and discussion

The biochar was initially produced through pyrolysis of chilli plants and chilli fruits at two different temperatures (600 °C and 800 °C). Yield is essential for evaluating the scalability of the synthetic process and determining the amount of raw waste material converted into biochar. The data in Table S1 show a decreasing yield with increasing temperature, consistent with findings from other studies,[43] though the yield always remains above 25 %. This indicates that the process of producing carbon materials from waste plant and fruit biomass can potentially be scaled up efficiently. The transition metal-functionalized biomass-derived electrocatalysts were synthesized via pyrolysis of biochar mixed with the respective metal precursors. This approach was used to achieve atomically dispersed nitrogen-coordinated iron (Fe-N_x) active sites for ORR electrocatalysts, and nickel nanoparticles for HER electrocatalysts. The morphological characteristics of the electrocatalysts were carefully examined using SEM images (Figure S1). The samples consist of individual or clustered particles with irregular shapes. These particles exhibit a high surface roughness and are marked by sharp, jagged edges. For the qualitative analysis of synthesized electrocatalysts, X-ray fluorescence (XRF) was carried out and the spectra were collected as displayed in Figs. 2a and 2b. All electrocatalyst samples exhibited distinct peaks corresponding to the targeted metals, specifically Fe or Ni, demonstrating the successful synthesis process. However, trace amounts

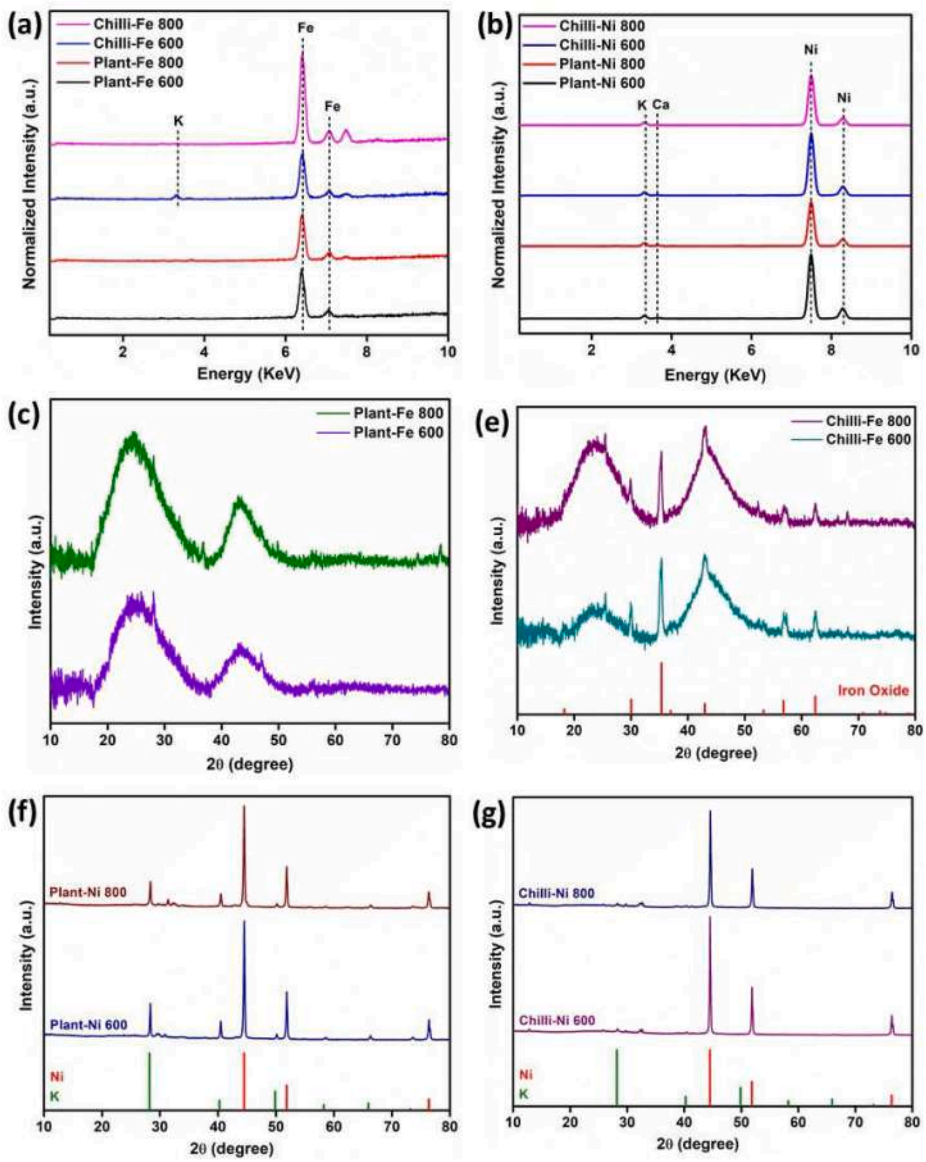

Fig. 2. XRF spectra of (a) iron functionalized biomass-derived carbon electrocatalysts and (b) nickel functionalized biomass-derived carbon electrocatalysts. XRD spectra of iron functionalized biomass derived from (c) plant and (d) chilli. XRD spectra of nickel functionalized biomass derived from (e) plant and (f) chilli.

of K, Ca, and Cl were detected in metal-functionalized biochar which are the essential micronutrients present in plants and fruits [44]. Notably, a distinct potassium peak is observed in the chilli-derived samples compared to the plant-derived samples. This can be attributed to the higher inherent potassium content in chilli fruits compared to the plant biomass [45] or an incomplete acid washing during activation for Fe-functionalized samples.

Furthermore, to investigate the phase and crystal structure of electrocatalysts, XRD analysis was executed and the diffraction patterns are depicted in Fig. 2c - 2*g*. Two broad diffraction peaks were observed for iron functionalized samples centered at 24° and 43° corresponding to (200) and (101) graphitic planes (JCPDS: 41–1487), respectively (Fig. 2c and 2d). Despite the iron functionalization, both Plant-Fe samples demonstrated diffraction peaks only corresponding to carbon with no distinct iron-related peaks. This absence could be attributed to the homogeneous distribution of iron within the biochar matrix, leading to a lack of separate crystalline iron phases that would produce distinct peaks or the iron-related peaks are masked by amorphous carbon peaks. Whereas Chilli-Fe samples consist of diffraction peaks related to iron oxide at around 25.4°, 29.8°, 35.3°, 43°, 52.3°, 56.8°, 62.4° and 68.1° which is consistent with magnetite (JCPDS:19–0629). The presence of iron oxide peaks in both samples indicates that iron not only integrates into the carbon matrix but also forms identifiable crystalline iron oxide phases. Notably, the formation of the magnetite phase after pyrolysis can be attributed to several factors inherent to the experimental setup and chemical environment. Although carbon exhibits reductive properties, the conditions of pyrolysis, particularly the presence of oxygen-containing functional groups within the activated biochar matrix and the controlled inert atmosphere play a crucial role in determining the final phase of composition [31,46]. Studies have demonstrated that during the pyrolysis of iron-functionalized biochar, interactions between iron precursors and oxygen species within the carbon matrix often result in the formation of iron oxides, including magnetite (Fe_3O_4) [47]. Along with this, the KOH activation process, while enhancing surface area and introducing structural defects, may also leave behind residual oxygen functionalities, further promoting the stabilization of iron in its oxidized form. Similar observations have been reported in studies of biochar functionalized with transition metals [48]. This coexistence of amorphous carbon and crystalline iron oxide phases could alter the material's catalytic properties by providing active sites for reactions while maintaining a conductive carbon network. However, nickel functionalized samples displayed sharp peaks at 44.5°, 51.8° and 76.3° corresponding to the characteristic diffraction lines of metallic Ni (JCPDS: 03–1051), signifying the presence of crystalline nickel phases in the biochar matrix (Fig. 2e and 2f). The absence of a carbon peak in the XRD patterns is due to the amorphous nature of the carbon matrix, which lacks a well-ordered graphitic structure and produces broad, low-intensity diffraction signals. Additionally, the presence of crystalline nickel phases dominates the XRD patterns, masking any weak signals from the amorphous carbon. The patterns also reveal peaks attributed to potassium (96–901–1977), which likely originates from the biomass itself and is carried forward through the pyrolysis and functionalization processes which is consistent with XRF results.

Raman spectroscopy was conducted to obtain detailed insights into the carbonaceous structure of the electrocatalysts, with the resulting spectra presented in Figure S2. All samples display two characteristic bands near 1341 cm^{-1} and 1577 cm^{-1}, referred to as the D and G bands, respectively. The G band is linked to the E_{2g} vibrational mode, representing the movement of sp^2 carbon atoms within the basal plane of an ideal graphitic lattice. Similarly, the D band arises from in-plane carbon vibrations near defects, associated with A_{1g} symmetry, indicating imperfections in the graphitic structure. The ratio of I_D/I_G, which reflects the level of defects in the carbon structure, was determined by dividing the intensity of the D band by that of the G band. An I_D/I_G value approaching one signifies a high degree of structural defects in the carbon. Notably, a linear relationship was observed between the I_D/I_G ratio and the temperature used during the initial pyrolysis. This finding suggests that higher pyrolysis temperatures may lead to an increase in structural defectivity [43,45]. The electron beam characterization of plant and chilli samples functionalized with iron was conducted at two pyrolysis temperatures (600 °C and 800 °C). STEM-EDX analysis revealed the presence of nanoparticles in all the samples (Fig. 3 and Fig. 4). Despite the broad range of particle sizes observed across the samples, nanoparticles in the plant samples were generally smaller than those in the chilli samples. The particle sizes ranged from 5 to 40 nm in the plant samples, while the chilli samples exhibited a larger size range of 5–120 nm. Pyrolysis temperature appeared to influence nanoparticle distribution, with the 600 °C samples containing a higher proportion of smaller particles and the 800 °C samples showing a shift toward larger particles. Among C, O and Fe, other elements such as Ca, K, Mg, S and Cl are visible (View Figure S3 and Figure S4), and seem to be present in the form of particles, where Mg and K maps superimpose mainly with Cl, Ca with O and S with Fe. N is still present in a very small amount. HR-TEM further supported the XRD results, confirming the absence of isolated iron in the samples. Fast Fourier Transform (FFT) analysis of the images showed diffraction patterns corresponding exclusively to the magnetite phase (Fig. 5). The electron beam characterization of Chilli-Ni 800 sample was conducted to extract significant insights into the morphology and elemental distribution of the nickel-functionalized biomass-derived electrocatalyst. The HAADF-STEM images (view Figure S5) reveal that nickel predominantly forms large aggregates, as evident from the bright, dense regions in the images. These particles are coupled with oxygen, as confirmed by the corresponding EDX elemental maps of C, O and Ni. Despite extensive imaging, no discernible lattice fringes were observed in the HR-TEM analysis. This absence can be attributed to the extreme thickness of the nickel aggregates, which hinders the resolution of internal crystallographic features. Additionally, the oxygen content around these aggregates is indicative of the high surface oxidation state, which is consistent with observations from XPS analysis.

Fig. 6 displays the XPS survey spectra of the plant and chilli-derived electrocatalysts treated at different temperatures (600 °C and 800 °C). The shake-up lines of C1s and O KLL signals are associated with peaks at around 320 eV and 980 eV, respectively, that are not highlighted in the figure. The calculated carbon (C1s) atomic percentages swing between 91.7 % for chilli-Fe 800 to 93.6 % for chilli-Fe 600 and from 92.0 % to 92.6 % for plant-Fe 800 and plant Fe-600, respectively. The nitrogen content is maximum for chilli-Fe 800 (3 %) and minimum for plant-Fe 600 (1.5 %). All the electrocatalysts have extremely low metal atomic percentages, with the largest total iron content of 0.4 % for chilli-Fe 600 and plant-Fe 800. Surprisingly, no other element has been encountered on the surface of the biomass-derived samples.

Fig. 7a-7d shows XPS spectra corresponding to N1s deconvolution peaks fitting the signals of imine (397.6 eV), pyridinic-N (398.3 eV), N_x-Fe (399.1 eV), pyrrolic-N (400.9 eV), and graphitic-N (402.2 eV) species, as reported in the literature for Fe-N-C compounds [11,43,45,49–51]. The relative percentage of N-Fe interactions was revealed to be: Plant-Fe 600 (51.13 %) > Plant-Fe 800 (47.80 %) > Chilli-Fe 600 (33.92 %) > Chilli-Fe 800 (26.5 %), whereas the trend for pyridinic/pyrrolic ratio was the opposite. Furthermore, imine peaks were not detected for all the electrocatalysts while graphitic nitrogen was found only for Plant Fe-800. However, the low overall N1s atomic percentage (see Fig. 6) is the cause of many spikes for the experimental curves associated with a notable inaccuracy of the fitting peaks.

Unquestionably, XPS on carbon (C1s) speciation is a more pertinent study that may be used to match the various species to ORR activity in alkaline conditions. In Fig. 8, the graphitic carbon is represented by the deconvoluted peak at 284.5 eV, the secondary carbons (C—N or C—O) at 285.0 eV, the CN_x defects at 286.2 eV, the C—OH/C—OC at 287.1 eV, the C = O at 288 eV, and the COOH at 289.4 eV. The highest relative percentage of graphitic carbon, in general, associated with low ORR activity, was achieved by the integration of the peak for Chilli-Fe 800

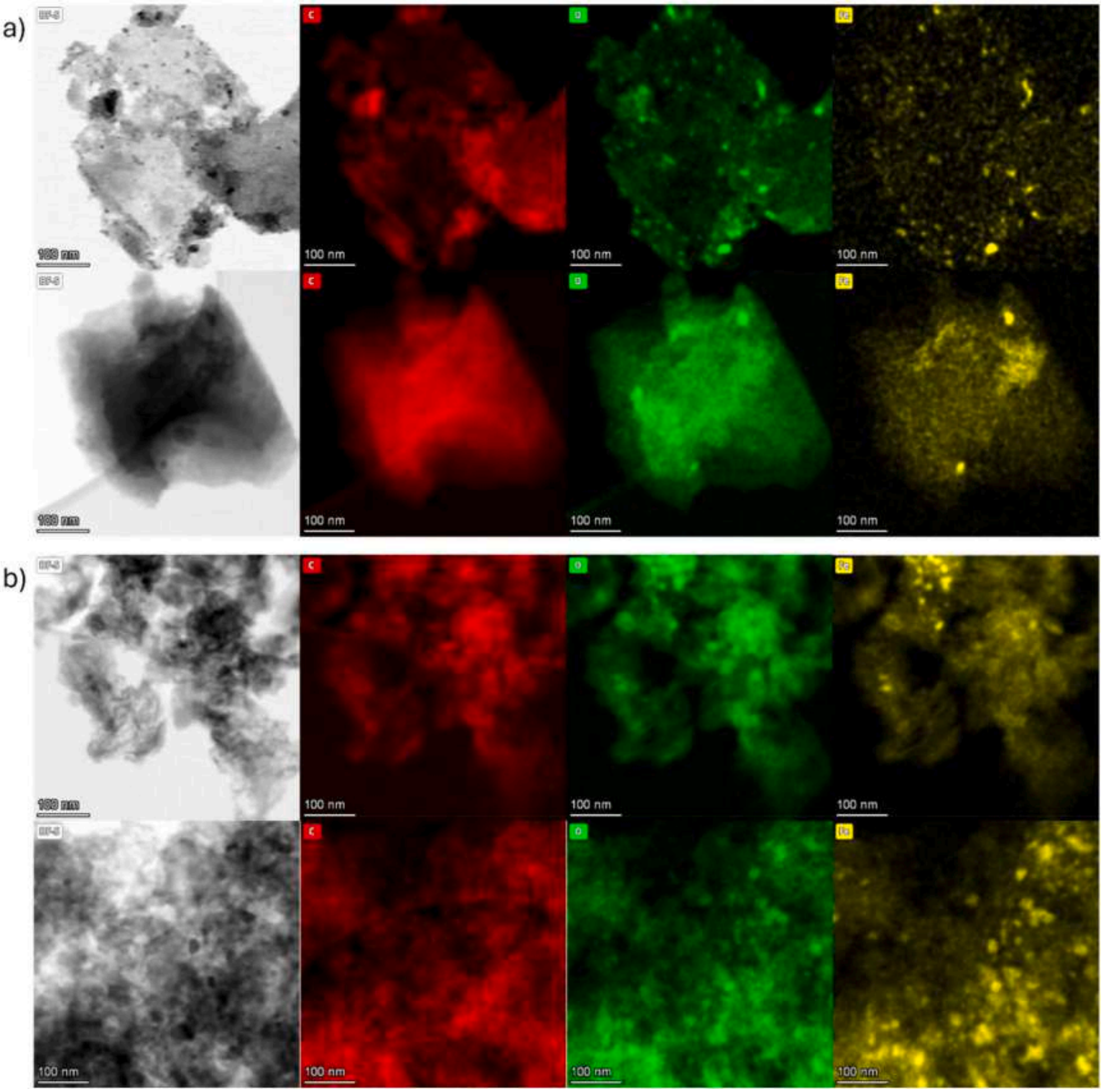

Fig. 3. STEM-EDX of the a) Plant-Fe 600 sample and b) Plant-Fe 800 sample. Columns, from left to right, report: Bright Field Image, C map, O map, Fe map.

catalyst (54.3 %), followed by Chilli-Fe 600 (48.5 %), Plant-Fe 800 (46.5 %), and Plant-Fe 600 (46.0 %). On the other hand, the largest relative percentage of C—N defects, normally correlated with high ORR activity, was reached by Plant-Fe 800 (13.6 %), followed by Plant-Fe 600 (10.3 %), Chilli-Fe 600 (9.9 %) and Chilli-Fe 800 (8.7 %).

For Chilli-Ni 800, high-resolution spectra for N1s and C1s are shown in Figure S6. The overall atomic percentage of nitrogen species in this sample was below 1 %, which is why the spectra appear scattered in Figure S6a. However, the pyrrolic-N signal dominates in the deconvoluted spectra, followed by the N—Ni interaction, graphitic-N, and pyridinic-N, respectively. In the C1s spectra, a significant contribution comes from oxidized compounds, particularly carboxylic groups (-COOH), due to the high atomic percentage of oxygen species on the surface. The high levels of oxidized compounds could be derived from the natural makeup of chilli biomass, which is rich in oxygen-containing functional groups. These groups might partially remain or re-form during the pyrolysis and functionalization processes [52,53]. Additionally, the pyrolysis temperature of 800 °C, while sufficient to remove many volatile compounds, may not entirely eliminate thermally stable oxygen functionalities, leaving a significant fraction of oxidized species intact on the biochar surface. From the integration of the deconvoluted peak areas, the relative percentage of graphitic or secondary carbons is approximately 16 %, with 9 % attributed to C—N defects.

In order to comprehend the responsiveness of biomass-derived electrocatalysts for ORR, electrochemical tests were carried out using RRDE, which gives information about the activity and selectivity of the electrocatalytic process through the reduction of hydrogen peroxide occurring on ringside. To simulate the employment of the developed electrocatalyst for anion exchange membrane fuel cells (AEMFCs), the tests were carried out in 0.1 M KOH alkaline electrolyte solution, corresponding to pH 13. LSV curves were recorded for both disk and ring electrodes at a rotation speed of 1600 rpm and a scan rate of 5 mV s^{-1}. The onset potential (E_{on}) and half-wave potential ($E_{1/2}$) were determined from the LSV of the disk current (J_{disk}) and are used as key performance indicators for the electrocatalytic activity. E_{on} is defined as the potential required to initiate the ORR, which was measured at −0.1 mA cm^{-2} according to current conventions in electrocatalysis [54]. $E_{1/2}$, which is located in the kinetic-mass transfer mixed regime, was determined by locating the maximum of the first derivative of the J_{disk} curve [55]. Additionally, the electrocatalyst can reach a current plateau known as the limiting current (J_{lim}).

Fig. 9 shows the ORR performance of iron-functionalized biomass-derived (final) carbon samples. The graphs illustrating the J_{disk} and I_{ring} curves are shown in Figs. 9a and 9b, respectively, while the peroxide percentage and the number of transferred electrons (n) are presented in Figs. 9c and 9d, respectively. Fig. 9a shows that the Plant-Fe samples

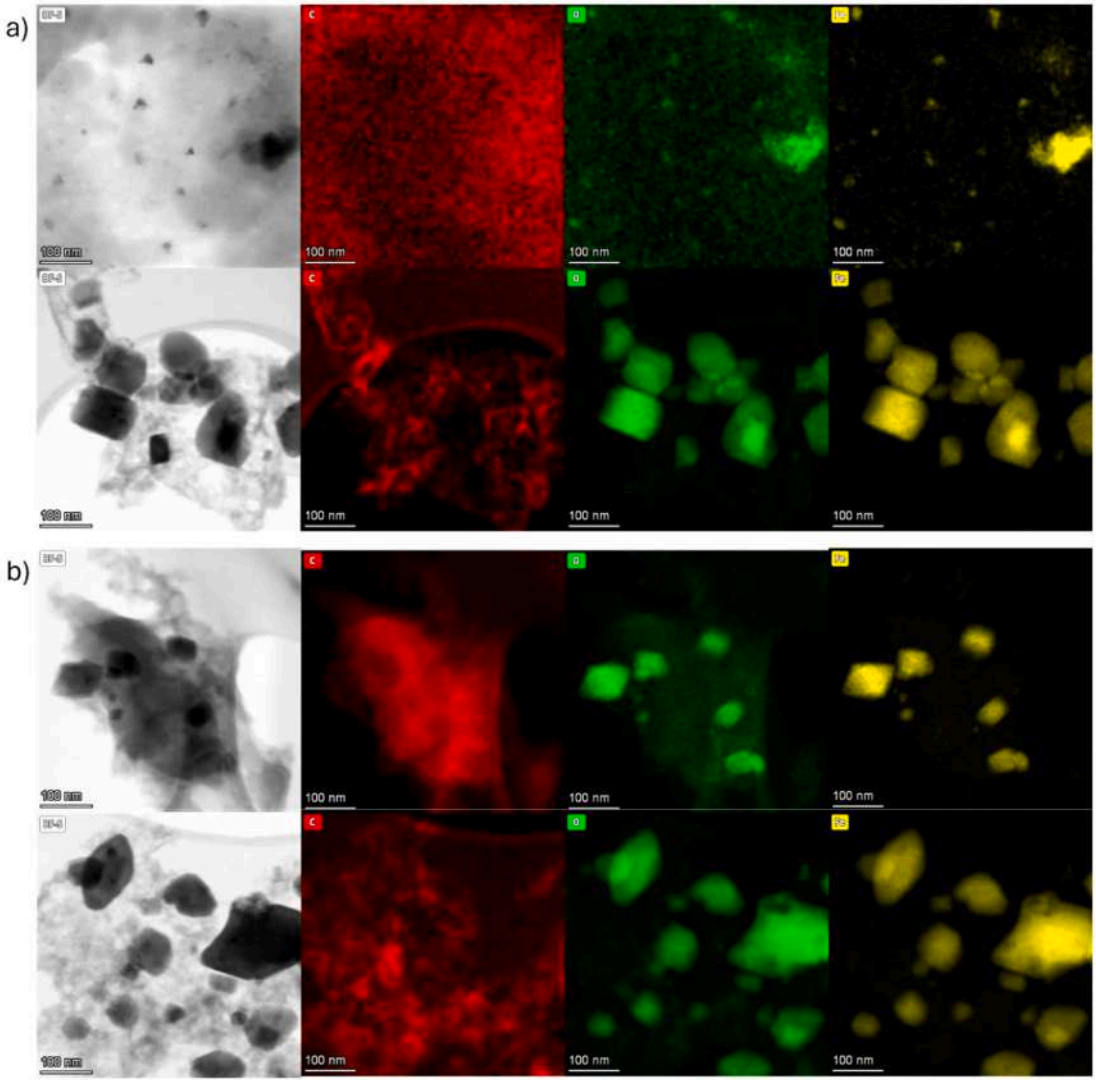

Fig. 4. STEM-EDX of the a) Chilli-Fe 600 sample and b) Chilli-Fe 800 sample. Columns, from left to right, report: Bright Field Image, C map, O map, Fe map.

exhibit higher currents in the diffusion-limited regime compared to the Chilli-Fe samples. This superior performance can be attributed to a higher density of Fe-N$_x$ active sites, as indicated by XPS analysis, and a better dispersion of iron within the carbon matrix. In particular, Plant-Fe 800 reaches the highest J_{lim} of 6.2, which corresponds to the (maximum) theoretical current value achievable by “perfect/ideal” ORR electrocatalyst [56]. Plant-Fe 600 exhibits a slightly lower limiting current. On the other hand, Chilli-Fe attains J_{lim} lower than 4.5 mA cm^{-2} and Chilli-Fe 600 exhibits the worst performance in J_{lim} (2.2 mA cm^{-2}), thus evidencing a strong (pyrolysis) temperature effect in Chilli-Fe samples. This outcome is much less prominent in Plant-derived carbons. Similarly, to J_{lim}, E_{on} declined according to the same trend, i.e., Plant-Fe 800 > Plant-Fe 600 > Chilli-Fe 600 > Chilli-Fe 800. $E_{1/2}$ follows instead a different trend, i.e., Plant-Fe 800 > Chilli-Fe 800 > Plant-Fe 600 and Chilli-Fe 600. The $E_{1/2}$ difference between the highest and the lowest value is 13 mV. With a remarkable onset potential of 0.97 V (vs RHE) and an outstanding half-wave potential of 0.87 V (vs RHE), Plant-Fe 800 proves to be the most active electrocatalyst which is comparable to those of commercial Pt/C catalysts under similar alkaline conditions, typically reported around 0.98–0.99 V (E_{on}) and 0.85–0.90 V ($E_{1/2}$) (Table 2) [57]. The peroxide % and n were calculated using J_{disk} and J_{ring}. Peroxide yield does not exceed 20 % and does not go below 3.6, respectively for all the electrocatalyst samples. This implies that all the electrocatalysts mostly undergo a direct 4-electron transfer bypassing the formation of HO_2^- intermediate. The significantly low peroxide production (below 10 %) and high number of electrons transferred (n > 3.8) along with the highest E_{on} and $E_{1/2}$ make Plant-Fe 800 a remarkable electrocatalyst for ORR and a promising candidate for the cathode material in AEMFCs. The performance differences among the synthesized electrocatalysts can be attributed to variations in Fe-N$_x$ content, pyrolysis temperature, and morphology. Samples processed at higher pyrolysis temperatures (800 °C) exhibited better electrocatalytic performance, as seen in Plant-Fe 800. This enhanced performance correlates with a higher surface area, as confirmed by SEM (Figure S1) and XPS analysis, which reveals an increase in graphitic carbon and nitrogen defect sites at elevated temperatures. STEM-EDX mapping (Fig. 3 and Fig. 4) further supports that Plant-derived biochar has a finer particle distribution, contributing to better mass transport and higher catalytic activity. The incorporation of Fe-N$_x$ active sites through functionalization with iron(II) phthalocyanine is pivotal, as these sites mimic the catalytic behavior of platinum group metals, facilitating efficient electron transfer during the ORR [13]. The nitrogen doping from the chilli-derived biochar further contributes by promoting electronic interactions that stabilize reaction intermediates, a feature supported by studies on similar nitrogen-doped biochar [35]. The Plant-Fe 800 catalyst stands out which could be due to its optimal balance between defect sites, Fe-N$_x$ coordination, and morphology, enabling superior electrochemical performance compared to other samples. To analyze the

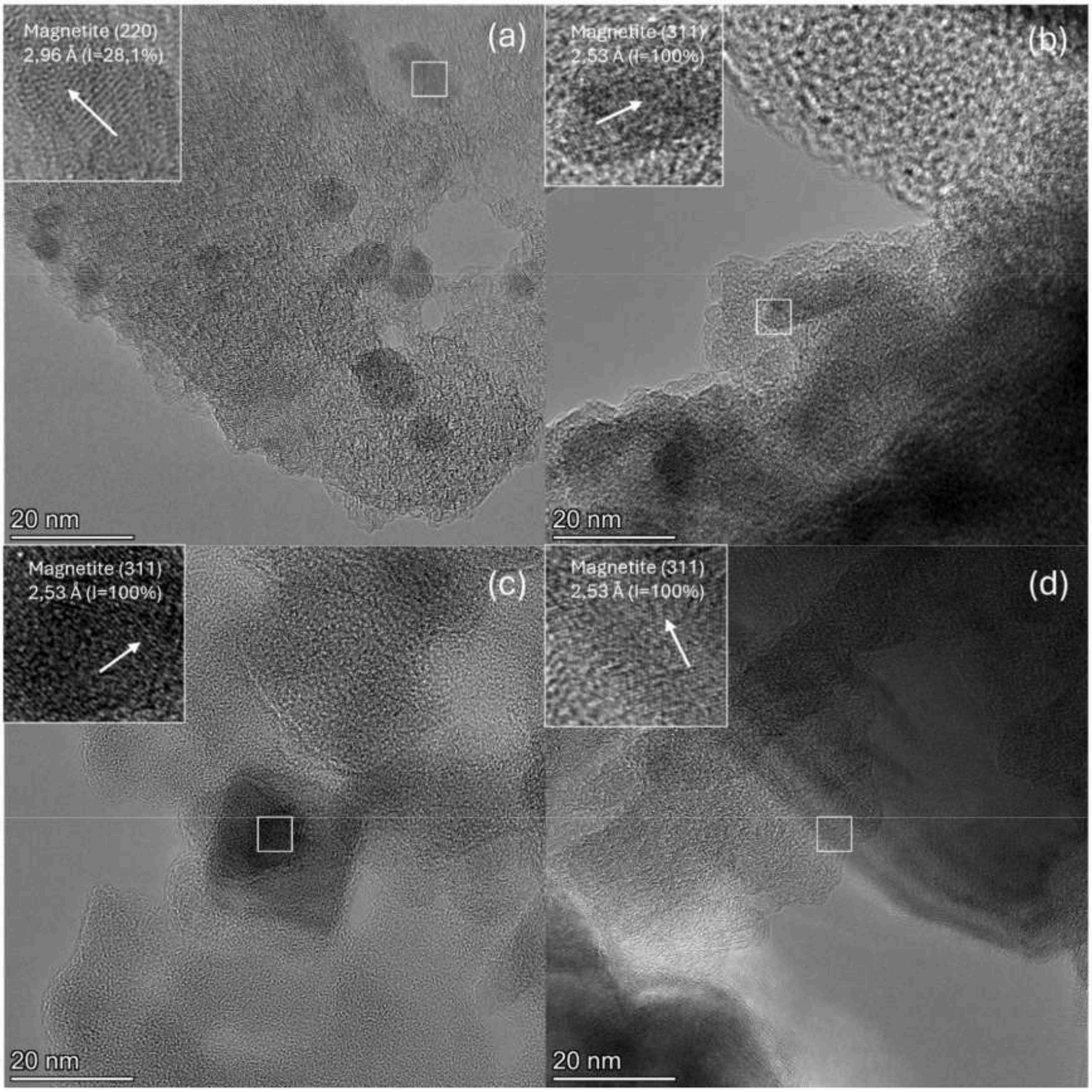

Fig. 5. HR-TEM images showing nanoparticles fine structure of a) Plant-Fe 600, b) Plant-Fe 800, c) Chilli-Fe 600 and d) Chilli-Fe 800.

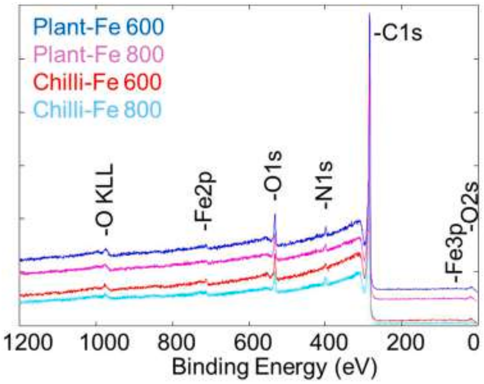

Fig. 6. XPS survey spectra of plant and chilli-based electrocatalysts.

durability of the electrocatalyst for ORR, an RRDE stability test of 2000 cycles was performed for the best-performing material Plant-Fe 800 and the results are displayed in Figure S7. The values of E_{on} and $E_{1/2}$ remained relatively stable during continuous potential cycling, however, an increase in the number of cycles led to a noticeable reduction in the limiting current density. As the cycling progressed, the ring current density exhibited a significant rise. Furthermore, the yield of peroxide anions, which is linked to both the disk and ring current measurements, showed a marked increase. Comparing the 2000th cycle to the 1st cycle revealed that the peroxide yield had almost doubled. Conversely, when examining the number of electrons transferred over the same cycles, a decrease was observed, dropping from 3.85 to 3.7. This observation highlights the electrocatalyst's kinetic durability under prolonged cycling conditions, despite the need for improvements in maintaining stable electron transfer efficiency and limiting current density over extended use. Table S2 presents a comparison of the ORR activity of Plant-Fe 800 with the recently reported biomass-derived electrocatalysts.

The nickel-functionalized biomass-derived carbon electrocatalysts were analyzed for HER using a RDE in 1 M KOH, where the electrode rotation was used to remove gas bubbles created during hydrogen production. The LSV was carried out from 0 to −1 V (vs RHE) at a scan rate of 5 mV/s and 1600 rpm of rotating disk speed to assess the HER activity of the electrocatalysts. The overpotential values were calculated at −10 mA cm^{-2} current density, according to the current literature protocol for HER electrocatalytic comparison [58,59]. Fig. 10 shows the HER polarization curves of all the electrocatalysts. The char derived from chilli plant and fruit biomass shows the lowest HER activity with

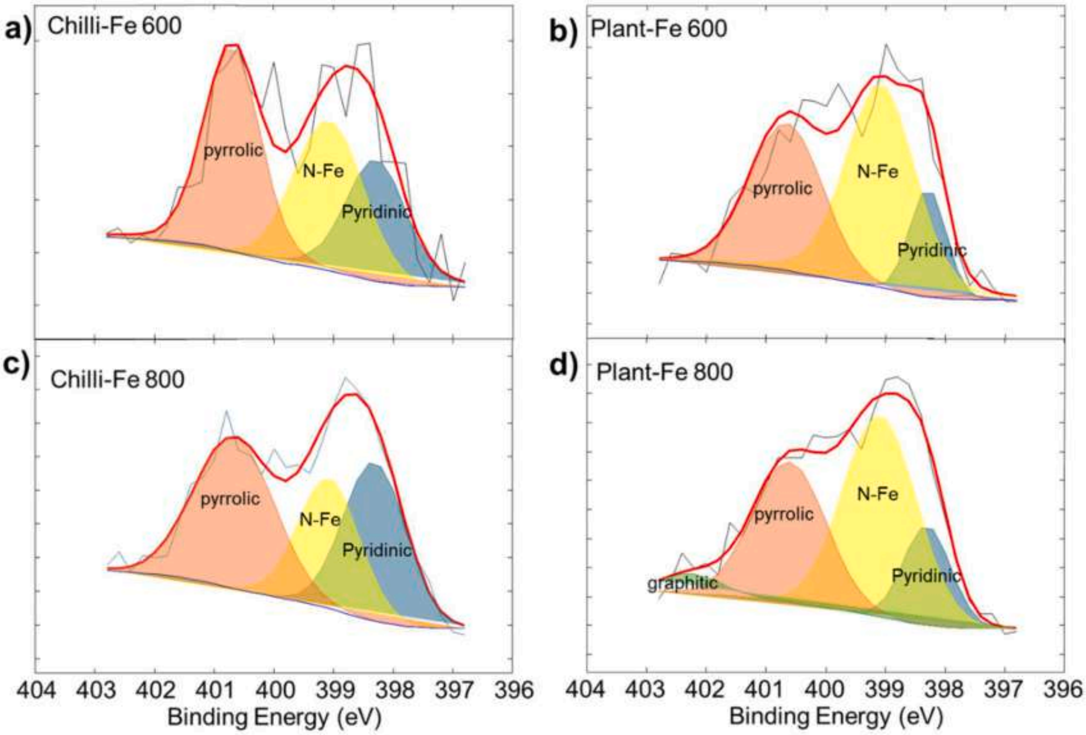

Fig. 7. Comparison of XPS N1s signal for a) Chilli-Fe 600, b) Plant-Fe 600 c) Chilli-Fe 800, and d) Plant-Fe 800.

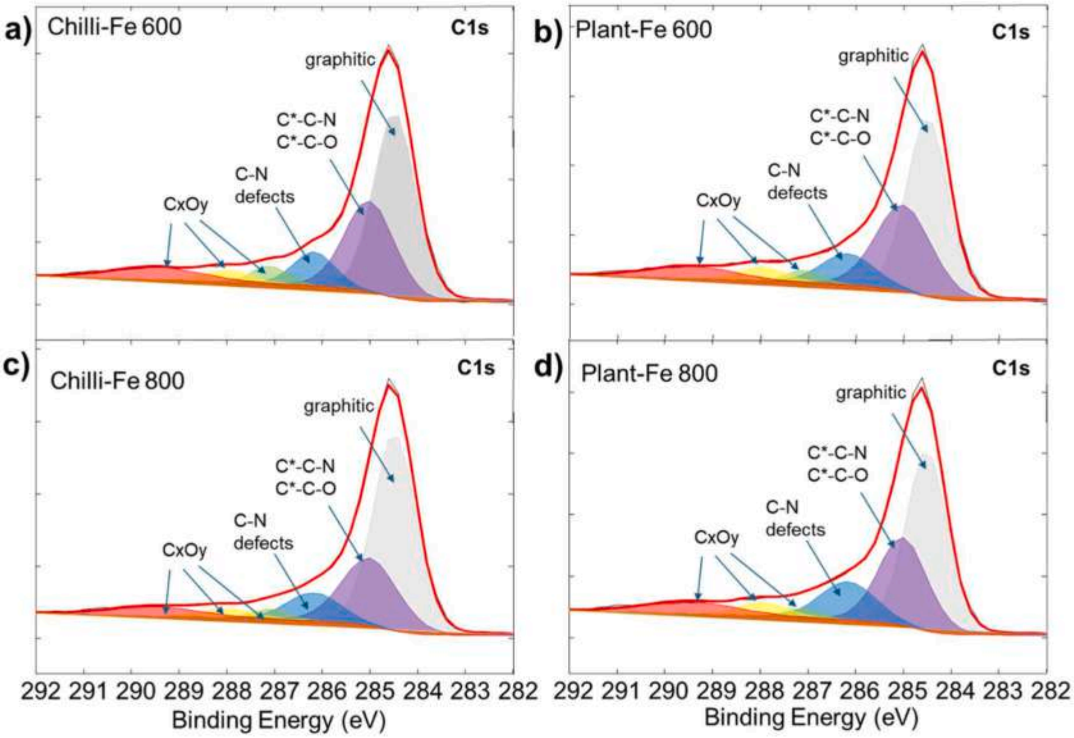

Fig. 8. Comparison of XPS C1s signal for a) Chilli-Fe 600, b) Plant-Fe 600 c) Chilli-Fe 800, and d) Plant-Fe 800.

overpotentials of more negative value than −0.7 V (vs RHE). However, the overpotentials were further reduced, and the HER activity increased after functionalizing the electrocatalysts with nickel. The overpotential values of nickel-functionalized electrocatalysts follow this trend: Chilli-Ni 800 > Chilli-Ni 600 > Plant-Ni 600 > Plant-Ni 800. Among these, Chilli-Ni 800 shows the highest activity with the lowest overpotential value of −0.41 V (vs RHE) (Table 3). Table S3 compares the HER activity of Chilli-Ni 800 with other recently reported electrocatalysts having biomass origin. Although the HER performance improved after Ni functionalization, it is still not comparable to commercially used platinum, having <100 mV of overpotential at −10 mA cm^{-2} [59]. However, while the current methodology of direct

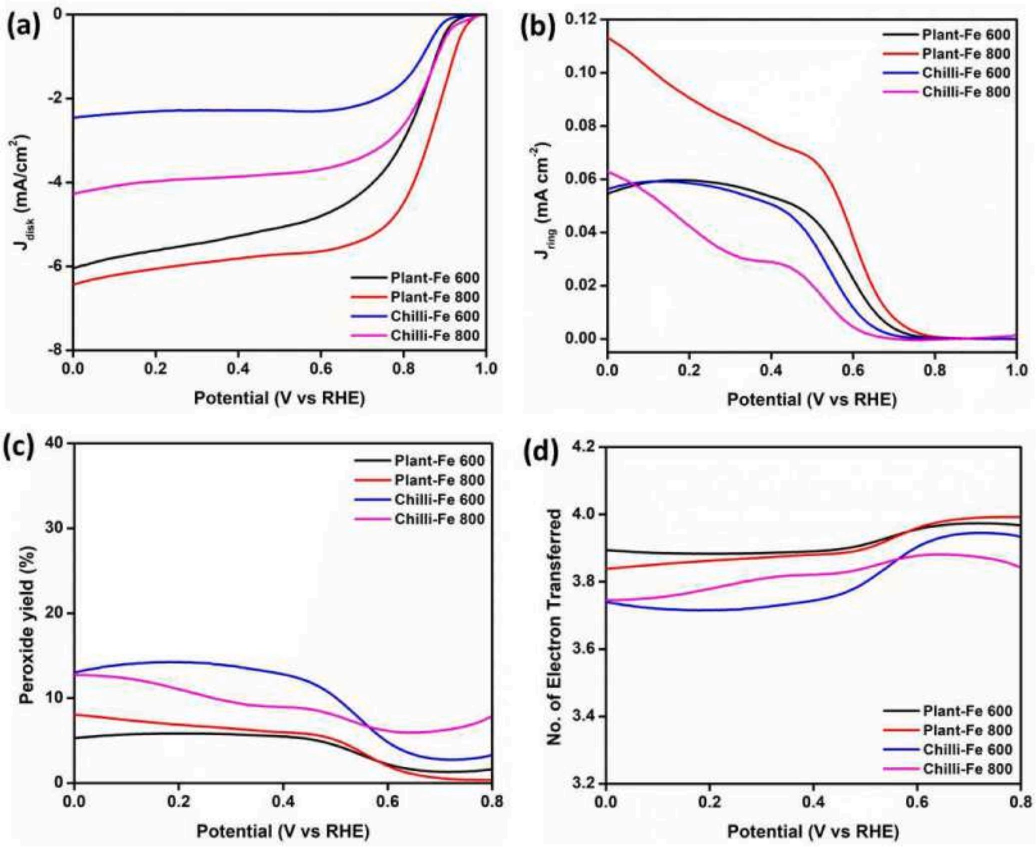

Fig. 9. RRDE measurements of synthesized electrocatalysts. (a) Disk current densities, (b) ring current densities, (c) peroxide yield and (d) number of electrons transferred during ORR.

Table 2
ORR electrochemical data of iron functionalized electrocatalysts listing E_{on} and $E_{1/2}$.

Electrocatalyst	E_{on} (V vs RHE)	$E_{1/2}$ (V vs RHE)
Plant-Fe 600	0.957	0.876
Plant-Fe 800	0.969	0.868
Chilli-Fe 600	0.928	0.873
Chilli-Fe 800	0.915	0.863

mixing of nickel nanopowder with biochar has demonstrated significant enhancement in HER activity, an alternative approach involving the pyrolysis of thermally degradable nickel salts in a reducing atmosphere could be explored in future studies to further enhance the HER performance. To test the durability of HER electrocatalyst, an RDE stability analysis of 2000 cycles with the scan rate of 50 mV s^{-1} was performed for the best-performing material Chilli-Ni 800 and the results are displayed in Figure S8. The polarization curve displayed a slight increase in the overpotential value from 410 mV to 470 mV after 2000 cycles. This study showcases the robustness of the nickel-functionalized biomass-derived carbon electrocatalyst in maintaining performance over extended cycling, highlighting the significance of biomass-derived electrocatalysts for long-term hydrogen evolution reactions in industrial applications.

4. Conclusion

Four electrocatalysts were synthesized from biochar derived from chilli plants and fruits, and pyrolyzed at 600 °C and 800 °C. The activation with KOH and subsequent functionalization with iron(II) phthalocyanine and nickel nanopowder produced highly porous, defect-rich carbon structures for ORR and HER, respectively. Notably, the Plant-Fe 800 catalyst exhibited exceptional ORR performance, with an $E_{1/2}$ of 0.87 V vs RHE and E_{on} of 0.97 V vs RHE. The catalyst demonstrated superior selectivity with peroxide production below 10 % and a high electron transfer number ($n > 3.8$), making it a more efficient and selective alternative to Pt-based catalysts. Similarly, the Chilli-Ni 800 electrocatalyst showed significant HER activity with a low overpotential of −0.4 V vs RHE, although further optimization is needed to match the performance of state-of-the-art platinum-based catalysts. Nevertheless, this study marks a pioneering effort in utilizing chilli-derived biochar for electrocatalyst development which has the potential for large-scale application in the future.

CRediT authorship contribution statement

Sumanth Dongre S: Writing – original draft, Methodology, Investigation, Funding acquisition, Formal analysis, Data curation. **Giovanni Zuccante:** Writing – original draft, Supervision, Data curation. **Mohsin Muhyuddin:** Writing – review & editing, Writing – original draft, Investigation, Formal analysis, Data curation. **Carmelo Lo Vecchio:** Writing – review & editing, Writing – original draft, Methodology, Investigation, Formal analysis, Data curation. **Vincenzo Baglio:** Writing – review & editing, Writing – original draft, Investigation, Formal analysis. **Enrico Berretti:** Writing – review & editing, Writing – original draft, Methodology, Investigation, Formal analysis, Data curation. **Alessandro Lavacchi:** Writing – review & editing, Writing – original draft, Methodology, Formal analysis, Data curation. **Shwetharani R:** Writing – review & editing, Writing – original draft, Supervision, Investigation. **R. Geetha Balakrishna:** Writing – review & editing, Writing – original draft, Supervision, Investigation. **Carlo Santoro:** Writing – review & editing, Writing – original draft, Supervision,

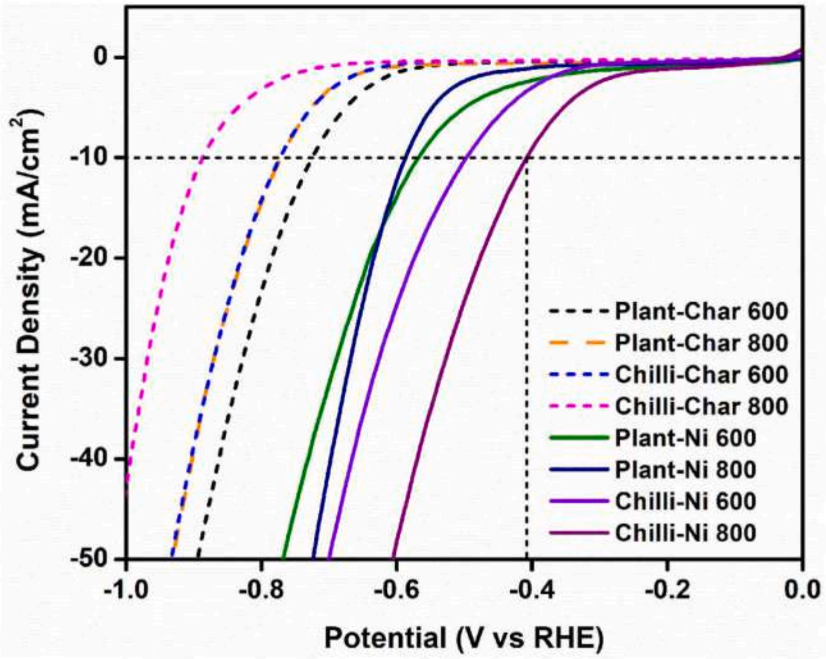

Fig. 10. RDE measurements of synthesized electrocatalysts. The linear sweep voltammograms of biomass-derived char and its nickel functionalized counterparts.

Table 3
HER electrochemical data of nickel functionalized electrocatalysts listing overpotential values.

Electrocatalyst	Overpotential (V vs RHE)
Plant-Char 600	−0.72
Plant-Char 800	−0.77
Chilli-Char 600	−0.77
Chilli-Char 800	−0.88
Plant-Ni 600	−0.56
Plant-Ni 800	−0.58
Chilli-Ni 600	−0.49
Chilli-Ni 800	−0.41

Methodology, Investigation, Funding acquisition, Conceptualization.

Declaration of competing interest

The authors declare that they have no known competing financial interests or personal relationships that could have appeared to influence the work reported in this paper.

Acknowledgements

S.D.S. gratefully acknowledges the financial support from the MAECI Visiting Fellowship awarded by the Ministry of Foreign Affairs and International Cooperation (MAECI), Italian Government. E.B. acknowledges the Circular and Sustainable Made in Italy Extended Partnership (MICS), funded by the European Union Next-Generation EU (Piano Nazionale di Ripresa e Resilienza (PNRR) - Missione 4, Componente 2, Investimento 1.3 - D.D. 1551.11-10-2022, PE00000004) for financial support. G.Z. acknowledges a Ph.D. scholarship on the Italian National Ph.D. program “Scientific, technological and social methods enabling circular economy”, Curriculum “Technical materials for circularity” funded by Italy’s Recovery and Resilient Plan and EU Recovery Plan

C.S. would like to acknowledge the NextGeneration EU from the Italian Ministry of Environment and Energy Security POR H2 AdP MMES/ENEA with involvement of CNR and RSE, PNRR - Mission 2, Component 2, Investment 3.5 "Ricerca e sviluppo sull’idrogeno” under the ENEA – UNIMIB agreement (Procedure 1.1.3 PNRR POR H2). M.M. would like to thank the Cariplo Foundation Call for Circular Economy through the project “Transformation of plastic waste in Electrocatalysts, Supported by exhausted gases recovery Layout” (TESLA) for the support.

Supplementary materials

Supplementary material associated with this article can be found, in the online version, at doi:10.1016/j.electacta.2025.145763.

Data availability

Data will be made available on request.

References

[1] A.P. Murthy, J. Madhavan, K. Murugan, Recent advances in hydrogen evolution reaction catalysts on carbon/carbon-based supports in acid media, J. Power. Sources. 398 (2018) 9–26, https://doi.org/10.1016/j.jpowsour.2018.07.040.
[2] A.M. Oliveira, R.R. Beswick, Y. Yan, A green hydrogen economy for a renewable energy society, Curr. Opin. Chem. Eng. 33 (2021) 100701, https://doi.org/10.1016/j.coche.2021.100701.
[3] Q. Hassan, S. Algburi, A.Z. Sameen, H.M. Salman, M. Jaszczur, Green hydrogen: a pathway to a sustainable energy future, Int. J. Hydrogen. Energy 50 (2024) 310–333, https://doi.org/10.1016/j.ijhydene.2023.08.321.
[4] B. Panigrahy, K. Narayan, B. Ramachandra Rao, Green hydrogen production by water electrolysis: a renewable energy perspective, Mater. Today: Proceedings 67 (2022) 1310–1314, https://doi.org/10.1016/j.matpr.2022.09.254.
[5] S. Shiva Kumar, H. Lim, An overview of water electrolysis technologies for green hydrogen production, Energy Reports 8 (2022) 13793–13813, https://doi.org/10.1016/j.egyr.2022.10.127.
[6] M. Singla, P. Nijhawan, D.A.S. Oberoi, Hydrogen fuel and fuel cell technology for 61a cleaner future: 61a review, Environ. Sci. Pollution Res. (2021) 28, https://doi.org/10.1007/s11356-020-12231-8.
[7] R.G. Bodkhe, R.L. Shrivastava, V.K. Soni, R.B. Chadge, A review of renewable hydrogen generation and proton exchange membrane fuel cell technology for sustainable energy development, Int. J. Electrochem. Sci. 18 (5) (2023) 100108, https://doi.org/10.1016/j.ijoes.2023.100108.
[8] L. Fan, Z. Tu, S.H. Chan, Recent development of hydrogen and fuel cell technologies: a review, Energy Reports 7 (2021) 8421–8446, https://doi.org/10.1016/j.egyr.2021.08.003.
[9] M.A. Abdelkareem, T. Wilberforce, K. Elsaid, E.T. Sayed, E.A.M. Abdelghani, A. G. Olabi, Transition metal carbides and nitrides as oxygen reduction reaction catalyst or catalyst support in proton exchange membrane fuel cells (PEMFCs), Int. J. Hydrogen. Energy 46 (45) (2021) 23529–23547, https://doi.org/10.1016/j.ijhydene.2020.08.250.
[10] L. Lin, P. Sherrell, Y. Liu, W. Lei, S. Zhang, H. Zhang, G.G. Wallace, J. Chen, Engineered 2D transition metal dichalcogenides—A vision of viable hydrogen

evolution reaction catalysis, Adv. Energy Mater. 10 (16) (2020) 1903870, https://doi.org/10.1002/aenm.201903870.

[11] S.A. Mirshokraee, M. Muhyuddin, J. Orsilli, E. Berretti, A. Lavacchi, C. Lo Vecchio, V. Baglio, R. Viscardi, A. Zaffora, F. Di Franco, M. Santamaria, L. Olivi, S. Pollastri, C. Santoro, Mono-, bi- and tri-metallic Fe-based platinum group metal-free electrocatalysts derived from phthalocyanine for oxygen reduction reaction in alkaline media, Nanoscale 16 (13) (2024) 6531–6547, https://doi.org/10.1039/D4NR00575A.

[12] M. Muhyuddin, A. Friedman, F. Poli, E. Petri, H. Honig, F. Basile, A. Fasolini, R. Lorenzi, E. Berretti, M. Bellini, A. Lavacchi, L. Elbaz, C. Santoro, F. Soavi, Lignin-derived bimetallic platinum group metal-free oxygen reduction reaction electrocatalysts for acid and alkaline fuel cells, J. Power. Sources. 556 (2023) 232416, https://doi.org/10.1016/j.jpowsour.2022.232416.

[13] Q. Ma, H. Jin, J. Zhu, Z. Li, H. Xu, B. Liu, Z. Zhang, J. Ma, S. Mu, Stabilizing Fe–N–C catalysts as model for oxygen reduction reaction, Adv. Sci. 8 (23) (2021) 2102209, https://doi.org/10.1002/advs.202102209.

[14] M. Sun, D. Davenport, H. Liu, J. Qu, M. Elimelech, J. Li, Highly efficient and sustainable non-precious-metal Fe–N–C electrocatalysts for the oxygen reduction reaction, J. Mater. Chem. A 6 (6) (2018) 2527–2539, https://doi.org/10.1039/C7TA09187G.

[15] J. Wang, H. Kong, J. Zhang, Y. Hao, Z. Shao, F. Ciucci, Carbon-based electrocatalysts for sustainable energy applications, Prog. Mater. Sci. 116 (2021) 100717, https://doi.org/10.1016/j.pmatsci.2020.100717.

[16] J. Wang, J. Kim, S. Choi, H. Wang, J. Lim, A review of carbon-supported nonprecious metals as energy-related electrocatalysts, Small. Methods 4 (10) (2020) 2000621, https://doi.org/10.1002/smtd.202000621.

[17] M. Muhyuddin, S. Mostoni, H.C. Honig, L. Mirizzi, L. Elbaz, R. Scotti, M. D'Arienzo, C. Santoro, Enhancing electrocatalysis: engineering the Fe–Nx–C electrocatalyst for oxygen reduction reaction using Fe-functionalized silica hard templates, ACS. Appl. Energy Mater. 7 (24) (2024) 11691–11702, https://doi.org/10.1021/acsaem.4c01215.

[18] K. Singh, F. Razmjooei, J.-S. Yu, Active sites and factors influencing them for efficient oxygen reduction reaction in metal-N coordinated pyrolyzed and non-pyrolyzed catalysts: a review, J. Mater. Chem. A 5 (38) (2017) 20095–20119, https://doi.org/10.1039/C7TA05222G.

[19] L. Huo, C. Jin, K. Jiang, Q. Bao, Z. Hu, J. Chu, Applications of nickel-based electrocatalysts for hydrogen evolution reaction, Adv. Energy Sustain. Res. 3 (4) (2022) 2100189, https://doi.org/10.1002/aesr.202100189.

[20] Z. Angeles-Olvera, A. Crespo-Yapur, O. Rodríguez, J.L. Cholula-Díaz, L. M. Martínez, M Videa, Nickel-based electrocatalysts for water electrolysis, Energies (5) (2022) 15, https://doi.org/10.3390/en15051609.

[21] S.A. Mirshokraee, M. Muhyuddin, N. Pianta, E. Berretti, L. Capozzoli, J. Orsilli, F. D'Acapito, R. Viscardi, A. Cosenza, P. Atanassov, C. Santoro, A. Lavacchi, Ni-phthalocyanine derived electrocatalysts for oxygen reduction reaction and hydrogen evolution reaction: active sites formation and electrocatalytic activity, ACS. Catal. 14 (19) (2024) 14524–14538, https://doi.org/10.1021/acscatal.4c03814.

[22] Q. Wang, R. Guo, Z. Wang, D. Shen, R. Yu, K. Luo, C. Wu, S. Gu, Progress in carbon-based electrocatalyst derived from biomass for the hydrogen evolution reaction, Fuel 293 (2021) 120440, https://doi.org/10.1016/j.fuel.2021.120440.

[23] Y. Cao, Y. Sun, R. Zheng, Q. Wang, X. Li, H. Wei, L. Wang, Z. Li, F. Wang, N. Han, Biomass-derived carbon material as efficient electrocatalysts for the oxygen reduction reaction, Biomass Bioenergy 168 (2023) 106676, https://doi.org/10.1016/j.biombioe.2022.106676.

[24] S. Li, S.-H. Ho, T. Hua, Q. Zhou, F. Li, J. Tang, Sustainable biochar as an electrocatalysts for the oxygen reduction reaction in microbial fuel cells, Green Energy Environ. 6 (5) (2021) 644–659, https://doi.org/10.1016/j.gee.2020.11.010.

[25] A. Srikhaow, E.E. Win, T. Amornsakchai, T. Kiatsiriroat, P. Kajitvichyanukul, S. M. Smith, Biochar derived from Pineapple leaf non-fibrous materials and its adsorption capability for pesticides, ACS. Omega 8 (29) (2023) 26147–26157, https://doi.org/10.1021/acsomega.3c02328.

[26] H. Yuan, L. Deng, Y. Qi, N. Kobayashi, J. Tang, Nonactivated and activated biochar derived from bananas as alternative cathode catalyst in microbial fuel cells, ScientificWorldJournal. 2014 (2014) 832850, https://doi.org/10.1155/2014/832850.

[27] A. Ehsani, H. Parsimehr, Electrochemical energy storage electrodes from fruit biochar, Adv. Colloid. Interface Sci. 284 (2020) 102263, https://doi.org/10.1016/j.cis.2020.102263.

[28] N. Torres-Lara, A. Molina-Balmaceda, D. Arismendi, P. Richter, Peanut shell-derived activated biochar as a convenient, low-cost, ecofriendly and efficient sorbent in rotating disk sorptive extraction of emerging contaminants from environmental water samples, Green Analytical Chemistry 6 (2023) 100073, https://doi.org/10.1016/j.greeac.2023.100073.

[29] Q. Shi, W. Wang, H. Zhang, H. Bai, K. Liu, J. Zhang, Z. Li, W. Zhu, Porous biochar derived from walnut shell as an efficient adsorbent for tetracycline removal, Bioresour. Technol. 383 (2023) 129213, https://doi.org/10.1016/j.biortech.2023.129213.

[30] K. Weber, P. Quicker, Properties of biochar, Fuel 217 (2018) 240–261, https://doi.org/10.1016/j.fuel.2017.12.054.

[31] M. Gale, T. Nguyen, M. Moreno, K.L. Gilliard-AbdulAziz, Physiochemical properties of biochar and activated carbon from biomass residue: influence of process conditions to adsorbent properties, ACS. Omega 6 (15) (2021) 10224–10233, https://doi.org/10.1021/acsomega.1c00530.

[32] L. Zhang, X. Jiao, G. He, Z. Shen, W. Wang, Iron phthalocyanine decorated porous biomass-derived carbon as highly effective electrocatalyst for oxygen reduction reaction, J. Environ. Chem. Eng. 11 (3) (2023) 109676, https://doi.org/10.1016/j.jece.2023.109676.

[33] X. Chen, J. Sun, T. Guo, R. Zhao, L. Liu, B. Liu, Y. Wang, J. Li, J. Du, Biomass-derived carbon nanosheets coupled with MoO2/Mo2C electrocatalyst for hydrogen evolution reaction, Int. J. Hydrogen. Energy 47 (72) (2022) 30959–30969, https://doi.org/10.1016/j.ijhydene.2021.12.173.

[34] N.E. Nkosi, P.M. Thabede, N.D. Shooto, One pot synthesis of Fe3O4-chili carbon composite removing methylene blue, paracetamol and nickel ions from an aqueous solution, Case Stud. Chem. Environ. Eng. 10 (2024) 100800, https://doi.org/10.1016/j.cscee.2024.100800.

[35] I.S. Marques, B. Jarrais, R. Ramos, V.K. Abdelkader-Fernandez, A. Yaremchenko, C. Freire, D.M. Fernandes, A.F. Peixoto, Nitrogen-doped biochar-supported metal catalysts: high efficiency in both catalytic transfer hydrogenation of furfural and electrocatalytic oxygen reactions, Catal. Today 418 (2023) 114080, https://doi.org/10.1016/j.cattod.2023.114080.

[36] Cortés-Ferré, H.E.; Guajardo-Flores, D.; Romero-De La Vega, G.; Gutierrez-Uribe, J. A. Recovery of capsaicinoids and other phytochemicals involved with TRPV-1 receptor to re-valorize Chili Pepper waste and produce nutraceuticals. 2021, 4. DOI: 10.3389/fsufs.2020.588534.

[37] A.S. Santhosh, M. Umesh, Valorization of waste chilli stalks (Capsicum annuum) as a sustainable substrate for cellulose extraction: insights into its thermomechanical, film forming and biodegradation properties, BioMass Convers. Biorefin. (2024), https://doi.org/10.1007/s13399-024-05370-2.

[38] Y. Ma, H. Bao, X. Hu, R. Wang, W. Dong, Productions of phenolic rich bio-oil using waste chilli stem biomass by catalytic pyrolysis: evaluation of reaction parameters on products distributions, J. Energy Inst. 97 (2021) 233–239, https://doi.org/10.1016/j.joei.2021.05.004.

[39] R.-F. Segundo, D.L. Magaly, N.M. Otiniano, N. Soto-Deza, N. Terrones-Rodriguez, D.L. Mayra, C.-C. Luis, L.M. Angelats-Silva, Sustainable energy from pickled chili waste in microbial fuel cells, Processes (9) (2024) 12, https://doi.org/10.3390/pr12092028.

[40] M. Yasin, L. Li, M. Donovan-Mak, Z.-H. Chen, S.K. Panchal, Capsicum waste as a sustainable source of capsaicinoids for metabolic diseases, Foods. (4) (2023) 12, https://doi.org/10.3390/foods12040907.

[41] L.G. Espinosa-Alonso, M. Valdez-Morales, X. Aparicio-Fernandez, S. Medina-Godoy, F. Guevara-Lara, Vegetable by-products, Food Wastes By-products (2020) 223–266.

[42] D.-F. Chai, Y. Han, W. Zhang, G. Dong, Z. Zhang, L. Bai, D. Guo, Ni nanoparticles assembled on the surface of biomass-derived porous carbon as competitive candidates for the hydrogen evolution reaction, CrystEngComm. 25 (15) (2023) 2298–2306, https://doi.org/10.1039/D3CE00117B.

[43] G. Zuccante, M. Acciarri, C.L. Vecchio, I. Gatto, V. Baglio, N. Pianta, R. Ruffo, L. Navarini, C. Santoro, Oxygen reduction reaction platinum group metal-free electrocatalysts derived from spent coffee grounds, Electrochim. Acta 492 (2024) 144353, https://doi.org/10.1016/j.electacta.2024.144353.

[44] A. Stephen Okiemute, A. Ifeanyi Michael Smarte, A. Jeremiah, K. Sammy Lewis, Biochar Development as a catalyst and its application, in: B. Mattia, G. Mauro, T. Alberto (Eds.), Biochar, IntechOpen: Rijeka, 2022, p. Ch. 13.

[45] S.A. Mirshokraee, M. Muhyuddin, R. Lorenzi, G. Tseberlidis, C.L. Vecchio, V. Baglio, E. Berretti, A. Lavacchi, C. Santoro, Litchi-derived platinum group metal-free electrocatalysts for oxygen reduction reaction and hydrogen evolution reaction in alkaline media, SusMat 3 (2) (2023) 248–262, https://doi.org/10.1002/sus2.121.

[46] C.H. Tessmer, R.D. Vidic, L.J. Uranowski, Impact of oxygen-containing surface functional groups on activated carbon adsorption of phenols, Environ. Sci. Technol. 31 (7) (1997) 1872–1878, https://doi.org/10.1021/es960474r.

[47] M. Muhyuddin, E. Berretti, S.A. Mirshokraee, J. Orsilli, R. Lorenzi, L. Capozzoli, F. D'Acapito, E. Murphy, S. Guo, P. Atanassov, A. Lavacchi, C. Santoro, Formation of the active site structures during pyrolysis transformation of Fe-phthalocyanine into Fe-nx-C electrocatalysts for the oxygen reduction reaction, Appl. Catal. B: Environmental 343 (2024) 123515, https://doi.org/10.1016/j.apcatb.2023.123515.

[48] K. Muuli, R. Kumar, M. Mooste, V. Gudkova, A. Treshchalov, H.-M. Piirsoo, A. Kikas, J. Aruväli, V. Kisand, A. Tamm, A. Krumme, P. Moni, M. Wilhelm, K. Iron Tammeveski, Cobalt, and nickel phthalocyanine tri-doped electrospun carbon nanofibre-based catalyst for rechargeable zinc–Air battery air electrode, Materials (13) (2023) 16, https://doi.org/10.3390/ma16134626.

[49] Y. Liu, M. Su, D. Li, S. Li, X. Li, J. Zhao, F. Liu, Soybean straw biomass-derived Fe–N co-doped porous carbon as an efficient electrocatalyst for oxygen reduction in both alkaline and acidic media, RSC. Adv. 10 (12) (2020) 6763–6771, https://doi.org/10.1039/C9RA07539A.

[50] L. Xiao, Q. Yang, M.J. Wang, Z.X. Mao, J. Li, Z Wei, N-doped and Fe-, N-codoped carbon: tuning of porous structures for highly efficient oxygen reduction reaction, J. Mater. Sci. 53 (21) (2018) 15246–15256, https://doi.org/10.1007/s10853-018-2683-8.

[51] R. Gokhale, Y. Chen, A. Serov, K. Artyushkova, P. Atanassov, Direct synthesis of platinum group metal-free Fe-N-C catalyst for oxygen reduction reaction in alkaline media, Electrochem. commun. 72 (2016) 140–143, https://doi.org/10.1016/j.elecom.2016.09.013.

[52] J. Chen, J. Zhou, W. Zheng, S. Leng, Z. Ai, W. Zhang, Z. Yang, J. Yang, Z. Xu, J. Cao, M. Zhang, L. Leng, H. Li, A complete review on the oxygen-containing functional groups of biochar: formation mechanisms, detection methods, engineering, and applications, Sci. Total Environ. 946 (2024) 174081, https://doi.org/10.1016/j.scitotenv.2024.174081.

[53] S. Bakshi, C. Banik, D.A. Laird, Estimating the organic oxygen content of biochar, Sci. Rep. 10 (1) (2020) 13082, https://doi.org/10.1038/s41598-020-69798-y.

[54] L. Bouleau, S. Pérez-Rodríguez, J. Quílez-Bermejo, M.T. Izquierdo, F. Xu, V. Fierro, A. Celzard, Best practices for ORR performance evaluation of metal-free porous carbon electrocatalysts, Carbon. N. Y. 189 (2022) 349–361, https://doi.org/10.1016/j.carbon.2021.12.078.

[55] A. Bonakdarpour, T.R. Dahn, R.T. Atanasoski, M.K. Debe, J.R. Dahn, H2O2 Release during oxygen reduction reaction on Pt nanoparticles, Electrochem. Solid-State Lett. 11 (11) (2008) B208, https://doi.org/10.1149/1.2978090.

[56] G. Zhong, S. Xu, L. Liu, C.Z. Zheng, J. Dou, F. Wang, X. Fu, W. Liao, H. Wang, Effect of experimental operations on the limiting current density of oxygen reduction reaction evaluated by rotating-disk electrode, ChemElectroChem. 7 (5) (2020) 1107–1114, https://doi.org/10.1002/celc.201902085.

[57] M. Ruan, J. Liu, P. Song, W. Xu, Meta-analysis of commercial Pt/C measurements for oxygen reduction reactions via data mining, Chinese J. Catal. 43 (1) (2022) 116–121, https://doi.org/10.1016/S1872-2067(21)63854-8.

[58] A. Krishnan, A. Ajith, A.V. Krishnan, R.E. Saji, S. Syamli, S.M.A. Shibli, Ni-based electro/photo-catalysts in HER – a review, Surf. Interfaces 36 (2023) 102619, https://doi.org/10.1016/j.surfin.2022.102619.

[59] B. Jiang, S. Liu, L. Cheng, L. Zhou, H. Cui, M. Liu, M. Wen, C. Wang, W. Wang, S. Li, X. Sun, Mass synthesis of Pt/C catalysts with high Pt loading for low-overpotential hydrogen evolution, Int. J. Hydrogen. Energy 58 (2024) 268–278, https://doi.org/10.1016/j.ijhydene.2024.01.183.